

# Regulator scheme dependence of the chiral phase transition at high densities

Konstantin Otto,<sup>1,2,\*</sup> Christopher Busch,<sup>1,2,†</sup> and Bernd-Jochen Schaefer<sup>1,2,‡</sup>

<sup>1</sup>*Institut für Theoretische Physik, Justus-Liebig-Universität Gießen, 35392 Gießen, Germany*

<sup>2</sup>*Helmholtz Forschungsakademie Hessen für FAIR (HFHF), GSI Helmholtzzentrum für Schwerionenforschung, Campus Gießen, 35392 Gießen, Germany*

A common feature of recent functional renormalization group investigations of effective low-energy QCD is the appearance of a back-bending behavior of the chiral phase transition line at low temperatures together with a negative entropy density in the symmetric regime. The regulator scheme dependence of this phenomenon and the necessary modifications at finite densities are analyzed within a two-flavor quark-meson model. The flows at finite densities for three different regulators of three- or four-dimensional momenta are confronted to each other. It is found that the back-bending behavior and the negative entropy density can be traced back to the explicit momentum dependence of the regulator shape function. While it persists for the often-used three-dimensional flat regulator, it vanishes for Callan-Symanzik type regulators. This points to truncation artifacts in the lowest order of the derivative expansion. A careful theoretical as well as numerical exploration is given.

PACS numbers: 12.38.Aw, 11.30.Rd, 11.10.Wx, 05.10.Cc

## I. Introduction

Until now, the QCD phase structure at high densities and low temperatures is mostly an unknown territory. Several distinct phases are expected to exist in this regime making its phase structure extremely rich [1]. Examples of cold and dense strongly-interacting matter cover exotic phases of QCD such as crystalline color-superconductor, 2SC and color flavor locked (CFL) phases and even possibly spatially inhomogeneous phases, for reviews see e.g. [2, 3]. Most of these phases are difficult if possible at all to achieve in laboratory experiments. Available experimental data in this area of the phase diagram is still limited and has rather poor statistics, cf. the recent beam energy scans (BES) at RHIC in Brookhaven [4]. Several upcoming experimental facilities such as the CBM [5] or NICA [6] experiments were designed to fill the gap and to explore this region with higher statistics in the near future.

From a theoretical point of view, state-of-the-art lattice simulations at finite chemical potentials are hampered by a sign problem [7] such that alternative approaches are necessary to investigate the intermediate-density region of the phase diagram. Most widely utilized tools in this context are effective models that by sharing some important symmetries with QCD are expected to reflect some of its characteristic properties. A notable example is the quark-meson model, also known as a linear sigma model combined with quarks, wherein the effective low-energy couplings arise from the integration of gluonic degrees of freedom [8–10]. Despite the crude simplification compared to full QCD these models do incorporate important phenomena such as the spontaneous chiral symmetry breaking and its restoration at finite temperature and/or density. However, most often such effective model approaches are typically studied in mean-field approximations where important non-perturbative quantum and thermal fluctuations are neglected,

though they are of utmost relevance in particular in the vicinity of any phase transitions. The situation can be much improved by combining these models with functional methods like the functional renormalization group (FRG), Dyson-Schwinger equations (DSEs) and  $n$ -PI approaches, thus making contact with the underlying full QCD. These methods are an essential and very powerful framework in the study of such non-perturbative issues. Recent elaborate studies in the context of full QCD with the FRG [11] and the DSE [12, 13] or even combinations of both [14, 15] suggest the existence of a critical endpoint at intermediate chemical potentials and temperatures, implying a chiral phase transition from a crossover to a first-order transition at increasing density. However, in the high-density region the physics becomes more involved which makes the needed and necessary truncations in the functional approaches rapidly inapplicable. Due to the lack of feasible first-principle computations in this region one is mainly led to the reliance on some simplified truncations within the functional framework combined with effective theories so far [16, 17].

The spontaneous breaking of chiral symmetry and its restoration at finite density has been studied extensively with the FRG by several groups in the past, for a recent review see [18]. First applications also to neutron star physics have been made only recently [19–22]. A still open question, however, is posed by the back-bending behavior of the chiral transition line at smaller temperatures [23] and the simultaneous occurrence of a negative entropy densities beyond the chiral transition as firstly discussed in [24]. Therein, it was speculated that besides a truncation or scheme dependent artifact, this phenomenon could also be related to an incorrect assumed vacuum state of the FRG method, caused by, e.g., the formation of diquark condensates or the existence of inhomogeneous phases. The back-bending of the chiral transition line has also been found in other models [25, 26] as well as with different numerical solution methods such as the discontinuous Galerkin method [27, 28] or the global pseudospectral Chebyshev expansion method [29]. All these findings exclude numerical solution artefacts impressively. Hence, the back-bending behavior and the appearance of the negative en-

\* E-Mail:konstantin.otto@physik.uni-giessen.de

† E-Mail:christopher.busch@physik.uni-giessen.de

‡ E-Mail:bernd-jochen.schaefer@theo.physik.uni-giessen.de

tropy density seems to be reasoned in the structure of the corresponding flow equations. In this work, we will attempt to solve this riddle by investigating the regulator scheme dependence of the high-density chiral phase transition.

The paper is organized as follows: After a brief recapitulation of the employed functional renormalization group method in Sec. II the inherent regulator scheme dependence of the flow equations for four-dimensional quantum field theories in local potential approximation are addressed in Sec. III. The necessary modifications of the regulator at finite densities are elaborated in the following and the relation to the Silver Blaze property is summarized in a general framework. In the next Sec. IV a quark-meson model truncation for two flavors is introduced and the flow equations for three different regulator choices as well as a parameter fixing procedure are outlined. In Sec. V the regulator scheme dependence of the phase structure in local potential approximation is analyzed. The backbending of the chiral phase transition and its relation to the choice of the regulator is elucidated. We end with a detailed analysis of the decoupling of the fermions from the flow and conclude in Sec. VI. A discussion of regulator optimization and further details such as the employed numerical methods and a discussion on the pole proximity of the vacuum flows are collected in four appendices A-D.

## II. Functional Renormalization Group

In order to make this work self-contained, we briefly recapitulate here important ingredients of the FRG which are needed for the present analysis. For QCD-related recent reviews see Refs. [9, 18, 30–32], for a recent global review on physics applications of the FRG including QCD see [33]. As already mentioned the FRG is a suitable non-perturbative approach towards solving continuum quantum field theories. A modern realization of Wilson’s RG idea in terms of a functional differential equation for the 1PI effective average action  $\Gamma_k$  [34, 35] is known as the Wetterich equation [36]

$$\partial_t \Gamma_k[\phi] = \frac{1}{2} \text{Tr} \left[ \partial_t R_k \left( \Gamma_k^{(2)}[\phi] + R_k \right)^{-1} \right]. \quad (1)$$

Here,  $\Gamma_k^{(2)}[\phi]$  denotes the second functional derivative with respect to the given field  $\phi$  and  $t = \ln(k/\Lambda)$  is the logarithmic RG scale relative to an initial UV momentum cutoff scale  $\Lambda$ . The trace runs over the momenta and all inner spaces such as flavor, spin or Dirac space.

Eq. (1) is a functional partial differential equation for  $\Gamma_k$  with a one-loop structure and interpolates between the microscopic bare action  $S$  in the UV and the full macroscopic quantum effective action  $\Gamma = \Gamma_{k=0}$  in the infrared (IR). An important ingredient of Eq. (1) is the momentum regulator  $R_k$  in the inverse propagator. For real bosonic fields this quantity is introduced in the action  $\sim \int_p \phi(-p) R_k(p^2) \phi(p)$  and

refers to the regulator scheme of the flow equation.<sup>1</sup> It introduces the scale parameter  $k$  which describes the RG coarse-graining. The regulator has to fulfill some essential properties which are crucial for this work which is why its detailed discussion is postponed to the next section. Basically, it acts as an additional mass term to the low-momentum modes while the insertion term in the momentum loop, the scale derivative of the regulator  $\partial_t R_k$ , regularizes the ultraviolet modes, thus making the flow IR and UV finite. This satisfies the RG notion of successively integrating out quantum fluctuations in a shell around the momentum  $p \sim k$ . While the Wetterich equation is an exact functional equation, in practice any attempt at its solution relies on a truncation of the underlying functional  $\Gamma_k$ . One possible truncation scheme is an expansion of  $\Gamma_k$  in powers of derivatives in four-dimensional configuration space, which e.g. for a scalar theory with a real field  $\phi(x)$  reads

$$\Gamma_k[\phi] = \int d^4x \left[ V_k(\phi) + \frac{1}{2} Z_k(\phi) (\partial_\mu \phi)^2 + \mathcal{O}(\partial^4) \right]. \quad (2)$$

The leading order derivative expansion with a vanishing anomalous dimension  $Z_k \equiv 1$  provides the ansatz for the local potential approximation (LPA). Then, for a constant vacuum expectation value (VEV)  $\langle \phi \rangle := \phi_0$ , the two-point function always exhibits the canonical momentum form  $\Gamma_k^{(2)} = p^2 + m_k^2$  with the effective momentum-independent curvature mass  $m_k^2 = d^2 V_k(\phi)/d\phi^2|_{\phi=\phi_0}$ . In general, the scale dependent effective potential  $V_k$  assembles all momentum independent field fluctuations to infinite order and thereby dynamically modifies  $m_k^2$ .

## III. Regulator Schemes

Any truncation of the effective average action necessarily leads to a corresponding error. The possible types and sizes of such errors are influenced among others by the choice of a suitable regulator function so that this is an important ingredient in the FRG framework [37, 38].

We focus our investigation on four-dimensional, local relativistic quantum field theories and start with bosonic fields without chemical potential. In momentum space, the regulator  $R_k(p^2)$  has squared-mass dimension and depends on a single momentum argument. Any suitable regulator  $R_k(p^2)$  can in principle be chosen at will but should obey the following three restrictions:

1.  $\lim_{k^2/p^2 \rightarrow 0} R_k(p^2) = 0$
2.  $\lim_{p^2/k^2 \rightarrow 0} R_k(p^2) > 0$
3.  $\lim_{k \rightarrow \infty} R_k(p^2) \rightarrow \infty$ .

<sup>1</sup> In the following we employ the short-hand momentum integration notation

$\int_p \equiv \int \frac{d^d p}{(2\pi)^d}$  wherein the dimension  $d$  is fixed by the one of index  $p$ .

The first requirement reflects the RG property that high momentum modes are fully integrated out in the infrared. The vanishing of the regulator ensures the crossing of the coarse-grained  $\Gamma_k$  to the full quantum 1PI effective action  $\Gamma$ . As a side remark,  $R_k(p^2)$  should vanish sufficiently fast,  $\lim_{p^2/k^2 \rightarrow \infty} (p^2)^{(d-1)/2} R_k(p^2) = 0$ , to obtain finite loop integrals in  $d$  dimensions.

The second requirement can be seen as an IR regularization such that the effective propagator in LPA at vanishing field  $\Delta_k(p^2) = 1/(p^2 + R_k(p^2))$  remains finite for  $p^2 \rightarrow 0$ , therefore avoiding infrared divergences in the presence of massless modes.

The last requirement in Eq. (3) just fixes the classical (bare) action  $S$  in the UV, e.g., for an effective theory with a finite UV cutoff  $\Lambda$ .

For convenience, a regulator function  $R_k(p^2)$  that does not depend on additional parameters can be rewritten in terms of a dimensionless shape function  $r(y)$

$$R_k(p^2) = p^2 r(y) \quad \text{with} \quad y = p^2/k^2 \quad (4)$$

by means of the (massless) dimensionless inverse propagator

$$P^2(y) \equiv \frac{1}{k^2} \Delta_k^{-1}(p^2) = y[1 + r(y)]. \quad (5)$$

To minimize truncation errors, general optimization criteria for regulator functions have been developed and are briefly reviewed in App. A. They are typically designed to minimize the regulator dependency of physical observables in the infrared and explicit optimizations have so far only been conducted for flows at vanishing chemical potential.

Beyond these criteria further requirements can be necessary. Examples are the preservation of the Silver Blaze property at finite chemical potential (see next Sec. III A) or the Slavnov-Taylor identities in gauge field theories, see e.g. [33].

Furthermore, we will argue in this work that there are additional large regulator dependent truncation artifacts at small temperatures and nonzero chemical potentials which lead to a back-bending phenomenon of the chiral transition line and the corresponding occurrence of negative entropy densities.

### A. Regulators and the Silver Blaze constraint

At nonvanishing densities, we extend the definition of the regulator to include a possible dependence on the associated chemical potentials. This is necessary in general to ensure certain physical properties of the theory. An example is QCD with one chemical potential as an external parameter. For vanishing temperature this yields a certain characteristic of the  $n$ -point functions  $\Gamma^{(n)}$  often dubbed as the *Silver Blaze* property in the literature [39]. It states for a fixed vacuum state and  $\mu$  smaller than some critical chemical potential  $\mu_c$  that the free energy of, e.g., a fermionic system does not exhibit a  $\mu$ -dependence at zero temperature. The critical chemical potential is determined by the pole mass of the lightest particle  $\mu_c = m_{\text{pole}}$  carrying a finite charge associated with the corresponding chemical potential. This transfers to the correlation

functions such that the  $\mu$ -dependence of  $\Gamma^{(n)}$  is solely given by replacing the zero components of the four-momenta in the vacuum correlation functions with  $\mu$ -shifted zero components. This becomes trivial for, e.g., a free Dirac fermion with mass  $m$ : the inverse propagator with a chemical potential  $\mu$  can be rewritten as

$$\Gamma^{(2)}(p_1, p_2; \mu) = \frac{\delta(p_1 - p_2)}{i\not{p}_1 - \mu\gamma_0 + m} = \Gamma^{(2)}(\tilde{p}_1, \tilde{p}_2; 0) \quad (6)$$

where  $\tilde{p}_i := (p_i^0 + i\mu, \mathbf{p}_i)$  denote the shifted momenta. For higher  $n$ -point functions and  $\mu < \mu_c$  Silver Blaze generalizes to

$$\Gamma^{(n)}(p_1, \dots, p_n; \mu) = \Gamma^{(n)}(\tilde{p}_1, \dots, \tilde{p}_n; 0) \quad (7)$$

with  $\tilde{p}_i = (p_i^0 + ic_i\mu, \mathbf{p}_i)$ . The value of  $c_i$  determines how the corresponding field couples to the chemical potential. For example, augmenting the free Dirac theory with bosons via, e.g., a Yukawa interaction, one has  $c_i = 1$  for fermionic momenta and  $c_i = 0$  for bosonic ones. See [26, 40] for more details and a proof of the Silver Blaze property in the functional 2PI framework.

The Silver Blaze constraint is necessary for a consistent thermodynamic treatment in particular close to a phase transition at low temperatures. In the context of the FRG the preservation of Eq. (7) in the infrared can be ensured by extending it to all scales  $k$

$$\Gamma_k^{(n)}(p_1, \dots, p_n; \mu) = \Gamma_k^{(n)}(\tilde{p}_1, \dots, \tilde{p}_n; 0) \quad (8)$$

where the threshold  $\mu_{c,k} = m_{\text{pole},k}$  is now scale-dependent since it is determined by the running pole mass [41, 42].

This translates to a similar property of the fermionic regulator such that it becomes  $\mu$ -dependent:

$$R_k^F(p; \mu) = R_k^F(\tilde{p}; 0). \quad (9)$$

As a consequence, in any loop diagram the frequency component of the loop momentum can be shifted by  $-i\mu$  and the contour in the complex plane can be closed. If no poles exist inside the closed contour and all external momenta of the loop diagrams are also shifted the vacuum result will be recovered.

For example, for a free Dirac field the zero temperature flow equation for the effective fermionic potential  $U_k^F$  (i.e., the negative pressure) at finite  $\mu$  is given by the loop integral

$$\begin{aligned} \partial_t U_k^F &= -\text{tr} \int_{-\infty}^{\infty} \frac{dp_0}{2\pi} \int \frac{d^3p}{(2\pi)^3} \frac{\partial_t R_k^F(p; \mu)}{i\not{p} + m + R_k^F(p; \mu)} \\ &= -\text{tr} \int_{-\infty+i\mu}^{\infty+i\mu} \frac{dp_0}{2\pi} \int \frac{d^3p}{(2\pi)^3} \frac{\partial_t R_k^F(p; 0)}{i\not{p} + m + R_k^F(p; 0)} \end{aligned} \quad (10)$$

which demonstrates the complex momentum shift compared to the original vacuum flow.

While Eq. (9) poses a necessary condition for the fulfillment of the Silver Blaze property, it is not sufficient. To ensure a completely  $\mu$ -independent flow for  $\mu < \mu_c$  the running

threshold  $\mu_{c,k}$  must always be larger  $\mu_c$  such that the pole mass is approached from above in the infrared. This is actually a challenging restriction for the regulator since additional poles in the complex plane might be generated by the regulator [43]. An example is given by the exponential regulator  $r^{\text{exp}}(y) = 1/(\exp(y) - 1)$  which generates infinitely many complex propagator poles in the complex frequency plane.

Explicit computations with regulators fulfilling all those conditions typically constitute an arduous analytical and numerical task; see e.g. [44, 45] for applications. A simple way to circumvent these problems is to use dimensionally reduced (i.e., purely spatial) regulators. In four dimensions, a popular choice is a three-dimensional cutoff function regularizing only the spatial modes:

$$R_k^{3\text{d}}(\mathbf{p}^2) = \mathbf{p}^2 r(x), \quad R_k^{F,3\text{d}}(\mathbf{p}) = i\mathbf{p} r^F(x) \quad (11)$$

with  $x := \mathbf{p}^2/k^2$ . Any  $\mu$ -dependence vanishes due to the absence of the frequency argument. Theories in the presence of such regulators always retain the Silver Blaze property because Eq. (9) is trivially fulfilled. For such a regulator, the flow equation for the potential (10) becomes

$$\partial_t U_k^F = -4 \int_{\mathbf{p}} \frac{\mathbf{p}^2 (1 + r^F(x)) \partial_t r^F(x)}{2E_k(\mathbf{p})} \Theta(E_k(\mathbf{p}) - \mu) \quad (12)$$

with

$$E_k(\mathbf{p}) = \sqrt{\mathbf{p}^2 (1 + r^F(x))^2 + m^2}. \quad (13)$$

The  $\mu$ -dependence is solely determined by the Heaviside step function and since  $E_k(\mathbf{p}) > m$  for all momenta the Silver Blaze property is fulfilled as long as  $\mu < m$ .

We end this section with a remark: Although a dimensionally reduced 3d regulator breaks  $O(4)$  Euclidean spacetime symmetry only a minor quantitative impact on the thermodynamics is expected. Moreover, at very large densities it might be advantageous to waive the Silver Blaze property in favor of other regulator characteristics. This is discussed in [46] where a symmetric summation of the fluctuations around the Fermi surface with a Silver Blaze-violating regulator has been found to improve the findings for BCS-like theories.

#### IV. Application: Quark-Meson Model

As an explicit application of the above considerations we employ a chiral two-flavor quark-meson model for the effective action with both bosonic fields  $\sigma, \pi$  as well as fermionic fields  $\psi$ . This model is widely regarded as an effective low-energy truncation to QCD, cf. Refs. [8, 9, 18, 47–51]. Its action

$$\Gamma_k[\phi, \bar{\psi}, \psi] = \int d^4x \left[ \frac{Z_{k,\phi}}{2} (\partial_\mu \phi)^2 + U_k(\phi^2) - c\sigma + \bar{\psi} \left( Z_{k,\psi} \not{\partial} + \frac{g_k}{2} (\sigma + i\gamma_5 \boldsymbol{\tau} \cdot \boldsymbol{\pi}) \right) \psi \right] \quad (14)$$

includes a field- and scale-dependent effective chiral potential  $U_k(\phi^2)$  for the meson fields. The fields can be combined in the a  $O(4)$ -symmetric four-vector  $\phi = (\sigma, \boldsymbol{\pi})$  such that the chirally symmetric potential depends only on the radial length squared  $\phi^2$ . Spontaneous breaking of chiral symmetry occurs for a global minimum at non-zero field value,  $\langle \phi^2 \rangle \neq 0$ . One generally chooses for the ground state  $\langle \phi \rangle = (\sigma_0, \mathbf{0})$  wherein the radial mode  $\sigma_0 \sim \langle \bar{\psi} \psi \rangle$  is related to the order parameter for chiral symmetry breaking, the chiral condensate.

The (constituent) quark field  $\psi$  carries  $N_c = 3$  color degrees of freedom and interacts with the four (pseudo)scalar mesons, the  $\sigma$ -meson and the three pions  $\pi$ , through a color-blind but running Yukawa coupling  $g_k$ . The interaction is non-diagonal in flavor space, signified by the Pauli matrices  $\boldsymbol{\tau}$ , and ensures isospin and chiral  $SU(2)_V \times SU(2)_A$  symmetry.

The constant and scale-independent explicit chiral symmetry breaking term  $-c\sigma$  in Eq. (14) incorporates the effects of finite current quark masses and yields finite pion masses. Throughout the work this parameter is fixed to  $c = (120.73 \text{ MeV})^3$  yielding  $m_\pi = 138 \text{ MeV}$ .

The scale-dependent but field-independent bosonic and fermionic wavefunction renormalizations  $Z_{k,\phi}$  and  $Z_{k,\psi}$  as well as the Yukawa coupling  $g_k$  are needed to determine an approximate effective potential at the chiral symmetry breaking scale  $k_\chi$ . In the subsequent solution of the full flow in local potential approximation (LPA), which corresponds to a leading-order derivative expansion, they are set constant but the running of the full effective potential  $U_k(\phi^2)$  is taken into account. Details on the solution procedure are laid out in Sec. IV B.

#### A. Regulator Choices

As outlined in Sec. III, possible regulator artifacts might be more apparent at finite chemical potential. In order to test the impact of the regulator shape function especially on the back-bending property in the low-temperature phase diagram, three different regulator functions are considered in the following:

$$\text{(I)} \quad R_k^{\text{mass},4\text{d}}(p) = k^2 \Theta(k_\phi^2 - p^2) \quad (15)$$

$$\text{(II)} \quad R_k^{\text{mass},3\text{d}}(\mathbf{p}) = k^2 \Theta(k_\phi^2 - \mathbf{p}^2) \quad (16)$$

$$\text{(III)} \quad R_k^{\text{flat},3\text{d}}(\mathbf{p}) = (k^2 - \mathbf{p}^2) \Theta(k^2 - \mathbf{p}^2) \quad (17)$$

The regulators in Eqs. (15)–(17) are bosonic regulators. To retain chiral symmetry, the fermionic analogues are chosen as outlined in Eqs. (A8)–(A11).

(I) The first regulator is closely related to the Callan-Symanzik regulator  $R_k^{\text{CS}}(p^2) = k^2$  and will be referred to as *mass-like* regulator<sup>2</sup>. Due to the momentum-independent mass-like factor  $k^2$  in front of the  $\Theta$ -function, high momenta

<sup>2</sup> Strictly speaking, only the bosonic version is directly related to the Callan-Symanzik regulator. Due to chiral symmetry, the fermionic regulator has an additional non-trivial Dirac structure.



are never fully integrated out and don't decouple for Callan-Symanzik type flows. Thus, in a strict sense they are not Wilsonian flows, i.e., the notion of integrating out fluctuations in momentum shells does not apply. This results in relatively poor performance in critical exponents computations [52]. However, since the momentum dependence of the effective loop propagator  $(\Gamma_k^{(2)} + R_k)^{-1}$  is not modified by such a term, this regulator represents a reasonable testing ground for the present study and makes it a natural choice for a 4d regulator since many issues as discussed in Sec. III A can be circumvented. The problem of the missing UV regularization in the Callan-Symanzik regulator is solved by introducing a step function that suppresses the four-momenta larger than the compositeness scale  $k_\phi$  and serves as an initial UV scale for the theory. Phenomenologically speaking, at the compositeness scale the mesonic bound states of quark bilinears form; see Ref. [47, 53] for early applications of this regulator function. Thus,  $k_\phi$  presents a hard physical cutoff scale. Note that in a recent work [54] a novel flowing renormalization procedure was introduced which allows to cancel the explicit  $k_\phi$  dependence. However, the momentum argument of the step function in Eq. (15) turns problematic since an analytic continuation to complex frequencies for finite chemical potentials is not possible. Similar as in Ref. [47] we proceed by temporarily replacing the  $\Theta$ -function with a smeared-out version  $\Theta_\epsilon$ , assuming that such a continuation then exists. All Matsubara sums can be solved analytically and the flow for the potential splits into a vacuum and thermodynamic contribution

$$\partial_t U_k(\sigma^2, T, \mu) = \partial_t U_k^{\text{vac}}(\sigma^2) + \partial_t U_k^{\text{th}}(\sigma^2, T, \mu). \quad (18)$$

The vacuum contribution reads for  $\nu = 4N_c N_f$

$$\partial_t U_k^{\text{vac}} = k^2 \int_{\mathbf{p}} \Theta(k_\phi^2 - \mathbf{p}^2) \left( \frac{1}{p_0^2 + E_\sigma^2} + \frac{3}{p_0^2 + E_\pi^2} - \frac{\nu}{p_0^2 + E_\psi^2} \right) \quad (19)$$

with the quasi-particle energies  $E_i(\mathbf{p}) = \sqrt{\mathbf{p}^2 + k^2 + m_i^2}$  for the fields  $i \in \{\sigma, \pi, \psi\}$ . The corresponding masses are  $m_\sigma^2 = 2U'_k + 4\sigma^2 U''_k$ ,  $m_\pi^2 = 2U'_k$  and  $m_\psi^2 = (g\sigma/2)^2$ , wherein derivatives with respect to  $\sigma^2$  are denoted by a prime, i.e.,  $U'_k \equiv dU_k/d\sigma^2$ . An analytical integration of Eq. (19) is possible and straightforward.

The thermal part is given by

$$\partial_t U_k^{\text{th}} = k^2 \int_{\mathbf{p}} \left( \frac{n_B(E_\sigma, T)}{E_\sigma} + \frac{3n_B(E_\pi, T)}{E_\pi} + \frac{\nu [n_F(E_\psi, T, \mu) + n_F(E_\psi, T, -\mu)]}{2E_\psi} \right), \quad (20)$$

where  $n_B$  and  $n_F$  denote the standard Bose and Fermi distributions

$$n_B(E, T) = \frac{1}{e^{E/T} - 1}, \quad (21)$$

$$n_F(E, T, \mu) = \frac{1}{e^{(E-\mu)/T} + 1}.$$

Since only the vacuum flow requires a UV regularization the compositeness scale is not necessary in the UV finite thermal flow contribution. This means that the discontinuity of the step function can formally be sent to infinity,  $k_\phi \rightarrow \infty$ , and any contributions from additional poles of the smeared  $\Theta_\epsilon$  function can be safely ignored.

(II) For the three-dimensional version of the mass-like regulator  $R_k^{\text{mass}, 3d}$ , Eq. (16), the vacuum part of the flow does not exhibit the complete  $O(4)$  symmetry anymore:

$$\partial_t U_k^{\text{vac}} = \frac{k^2}{2} \int_{\mathbf{p}} \Theta(k_\phi^2 - \mathbf{p}^2) \left( \frac{1}{E_\sigma} + \frac{3}{E_\pi} - \frac{\nu}{E_\psi} \right). \quad (22)$$

The thermal flow contribution is identical to the previous 4d version, Eq. (20), with the exception that we do not take the limit  $k_\phi \rightarrow \infty$  because the  $\Theta$ -function only acts on spatial momenta and does not introduce any additional poles.

It should be noted that both mass-like regulators are not optimized according to any optimization criteria as discussed in App. A.

(III) The third regulator is the often-used flat regulator in three dimensions, also known as Litim regulator. It removes all spatial-momentum dependence from the loop propagator, such that the quasi-particle energies for the field  $i$  turn into  $E_i = \sqrt{k^2 + m_i^2}$ .

In contrast to Callan-Symanzik type flows, at a given scale  $k$  all fluctuations with (spatial) momenta larger than  $k$  are completely integrated out. The vacuum and thermal contributions take the simple forms

$$\partial_t U_k^{\text{vac}} = \frac{k^5}{12\pi^2} \left( \frac{1}{E_\sigma} + \frac{3}{E_\pi} - \frac{\nu}{E_\psi} \right), \quad (23)$$

and

$$\partial_t U_k^{\text{th}} = \frac{k^5}{6\pi^2} \left( \frac{n_B(E_\sigma, T)}{E_\sigma} + \frac{3n_B(E_\pi, T)}{E_\pi} + \frac{\nu (n_F(E_\psi, T, \mu) + n_F(E_\psi, T, -\mu))}{2E_\psi} \right). \quad (24)$$

## B. Parameter Fixing

For the explicit numerical solution of the flow equations an initial action needs to be fixed in the UV. Usually, in LPA the potential  $U_{k=\Lambda}$  is parameterized by some couplings for a given UV cutoff to reproduce physical observables in the infrared. Unfortunately, for the mass-like regulators this procedure could not be applied. A fixing of the potential up to some quartic couplings with a satisfactory chiral symmetry breaking scenario in the infrared was not possible since the needed numerical parameter space was not accessible. The pole structure of the threshold functions in the corresponding flow equations impedes the numerical handling in particular for the vacuum flow and close to the origin of the radial  $\sigma$ -field. In App. C more details and consequences of the pole proximity for different regulators are given.

However, we circumvent this issue and fix the initial action as follows: One feature of the quark-meson model truncation is the presence of a sort of an approximate partial IR fixed point in the symmetric regime above the chiral symmetry breaking scale  $k_\chi$ . All trajectories of the running couplings with initial values fixed at scales larger than  $k_\chi$  show a similar convergence behaviour. The partial fixed point behavior is inherited for heavy mesons from effective four-quark interactions generated in QCD [11, 49, 55] and can be used to fix the effective potential at  $k_\chi$ , see also [47, 56]. Due to the fixed-point behavior many infrared parameters of the action will be almost independent of their initial values since the system eventually loses its memory of the initial values fixed at the larger compositeness scale  $k_\phi > k_\chi$ . In addition, for large enough Yukawa couplings only a few relevant parameters need to be determined from QCD or alternatively from phenomenology. The physical IR fixed point at  $k \rightarrow 0$  can be estimated for scales in the symmetric regime  $k_\chi < k < k_\phi$  with the flow equations for both wavefunction renormalizations  $Z_{k,\phi}$  and  $Z_{k,\psi}$ , the Yukawa coupling  $g_k$ , and the effective potential  $U_k(\phi^2)$ . From the Landau pole of the renormalized Yukawa coupling in the vicinity of the compositeness scale  $k_\phi$  the mesons have large renormalized masses and the flows are dominated by the quarks following from the condition  $Z_{k,\phi} \ll 1$ .

It is therefore reasonable to consider only the purely fermionic contributions to the flows. The Yukawa coupling feeds back to the flow of the meson wavefunction renormalization whereas the fermionic anomalous dimension vanishes. The corresponding solution for the dimensionless effective potential

$$u_k(\tilde{\rho}) := \frac{U_k(\phi^2)}{k^4} \quad (25)$$

as a function of the dimensionless renormalized chiral invariant

$$\tilde{\rho} := Z_{\phi,k} \frac{\phi^2}{2k^2} \quad (26)$$

exhibits a partial infrared fixed point.

Assuming a power expansion of the potential around the origin

$$u_k(\tilde{\rho}) = \sum_{n=0}^{\infty} \frac{1}{n!} u_k^{(n)}(0) \tilde{\rho}^n, \quad (27)$$

infrared-attractive solutions for the scaled coefficients

$$\frac{u_k^{(2)}(0)}{\bar{g}_k^2} \quad \text{and} \quad \frac{u_k^{(n)}(0)}{\bar{g}_k^{2n}} \quad \text{for } n > 2 \quad (28)$$

can be found, where  $\bar{g}_k = Z_{k,\psi}^{-1} Z_{k,\phi}^{-1/2} g_k$  is the renormalized Yukawa coupling, cf. [56] for a similar analysis. Further technical details of the fixed-point solution are moved to App. B. At  $k_\chi$  the coefficient  $u_{k_\chi}^{(1)}(0)$  vanishes and the approximation of large renormalized meson masses breaks down. The other coefficients  $u_{k=k_\chi}^{(n)}(0)$  for  $n \leq 4$  are set to their infrared

fixed-point values and all higher orders  $n > 4$  are neglected. The  $n = 0$  coefficient is just a constant and can be ignored. From  $k_\chi$  downwards, the Yukawa coupling starts to freeze out. Hence, from this scale on the full flow is solved in LPA for a fixed Yukawa coupling  $g = \bar{g}_{k=k_\chi} = 6.5$  and vanishing anomalous dimensions. In principle, the only free parameter left is the symmetry breaking scale  $k_\chi$ . It can be fixed to yield the physical pion decay constant,  $\sigma_{\min} \approx f_\pi = 92.4 \text{ MeV}$  in the infrared.

For the mass-like regulators, Eqs. (15) and (16),  $k_\phi$  is an additional free parameter. The correct combination of the two parameters is not so clear since, for example, the sigma mass seems to only weakly depend on it.

The chosen parameter sets that seem to lie in a physically acceptable region are tabulated in Tab. I. The  $n = 2$  coefficient is regulator independent and is fixed to one at  $k_\chi$ . Note that the direct computation of the vacuum flow is not possible for the mass-like regulators due to the mentioned pole structure in the flow equation (see discussion in App. C). A numerical treatment, however, is possible at small temperatures and chemical potentials around the (pseudo)critical value  $\mu_c$ . By extrapolating into the Silver Blaze region we thus can infer approximate vacuum solutions. For the mass-like regulators we could not determine a precise vacuum sigma meson mass in this manner due to a strong  $\mu$  dependence around the critical  $\mu_c$ . For both regulators we nevertheless expect mass values around  $m_\sigma = 510 \text{ MeV}$  similar as the ones found for the flat regulator within an error of about 40 MeV.

Note that the assumption of a  $(T, \mu)$ -independent initial UV action only holds for sufficiently low external parameters much smaller than  $k_\chi$ , i.e.  $T \ll k_\chi$  as well as  $\mu < k_\chi$  [57].

Finally, we would like to emphasize that the sufficient memory loss of the initial values, i.e., the close proximity to the fixed point, is not yet necessarily satisfied at the chiral scale  $k_\chi$  in contrast to the statements in [56]. Therein it is indicated that the IR fixed point is already established at the chiral scale. However, for a ratio  $k_\chi/k_\phi \approx 1/2$ , which corresponds to an RG time of just  $t \approx -\ln(2)$ , the solutions show that the  $t \rightarrow -\infty$  fixed point is not nearly reached at this point.

Furthermore, the explicit  $k_\phi$ -dependence of the mass-like regulators leads to a modification of these solutions. Approximate IR fixed points still appear when  $k_\phi/k \rightarrow \infty$ , but the convergence to these values might be even slower. Nevertheless, we regard the explained procedure as a good choice for a testing ground, allowing for the comparison of different regulator schemes within a common setup and with only a few free parameters.

## V. Numerical Results

In this section, we focus on the phase boundary of the chiral phase transition at high densities. One of the first questions concerns the impact of a finite infrared cutoff  $k_{\text{IR}} > 0$  in the flow. In Fig. 1 the infrared scale dependence of the chiral phase diagram for the 3d flat regulator is demonstrated. A familiar back-bending of the transition line as well as a

|          | $k_\chi$ [MeV] | $k_\phi$ [MeV] | $u_{k_\chi}^{(3)}/\bar{g}_{k_\chi}^6$ | $u_{k_\chi}^{(4)}/\bar{g}_{k_\chi}^8$ |
|----------|----------------|----------------|---------------------------------------|---------------------------------------|
| mass, 4d | 480            | 690            | -0.00950                              | 0.00475                               |
| mass, 3d | 390            | 610            | -0.00950                              | 0.00475                               |
| flat, 3d | 580            | —              | -0.02375                              | 0.02078                               |

Table I. Chiral symmetry breaking scale  $k_\chi$  and compositeness scale  $k_\phi$  as well as starting parameters of the effective potential for the three different regulators. Evaluation of the  $u_k^{(n)}$  at  $\tilde{\rho} = 0$  is implied. Note that the infrared solutions for the mass-like regulators degenerate and the  $n = 2$  infrared attractive point is regulator independent resulting in  $u_{k_\chi}^{(2)}/\bar{g}_{k_\chi}^2 \equiv 1$ .

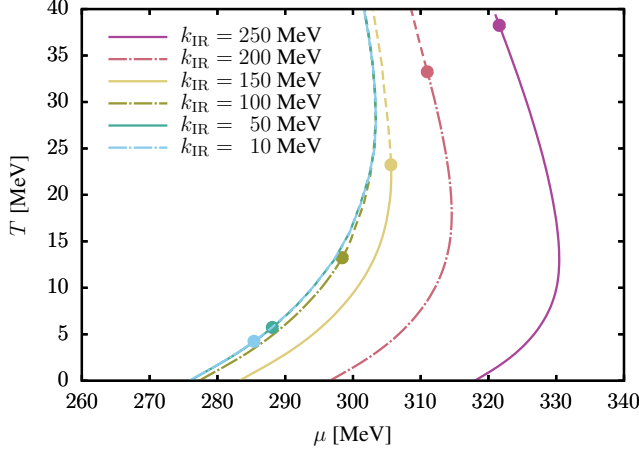


Figure 1. Infrared cutoff dependence of the chiral phase transition with the 3d flat regulator. Critical endpoints are marked by dots, solid and dash-dotted lines denote first-order and dashed lines crossover transitions.

movement of a critical endpoint towards lower temperatures is found with the consequence that the critical chemical potential moves to lower values. The back-bending occurs even at large infrared scales and is not related to the location of the critical endpoint. The flow in the infrared is dominated by the lightest degrees of freedom, the pions, which tend to restore the chiral symmetry. As a consequence, for scales below the pion mass,  $k_{\text{IR}} \lesssim 100$  MeV, the phase boundary consolidates. The movement of the critical endpoint can be traced back to the value of the sigma meson curvature mass in the infrared [48, 58] which does not freeze due to the running of the second derivative of the potential  $U_k''$ .

Hence, the back-bending is a generic feature of the employed truncation and regulator and not of the particular choice of the UV potential or IR cutoff. In the following, we will always use a fixed  $k_{\text{IR}} = 50$  MeV.

In Fig. 2 the regulator scheme dependence of the chiral phase boundary at low temperatures is presented. While the phase boundary obtained with the common 3d flat regulator exhibits a back-bending it vanishes for mass-like regulators. For both the 3d and 4d versions, the transition line hits the  $\mu$ -axis perpendicularly. This is already a strong hint that the back-bending in LPA is related to the momentum structure of the employed regulator. For both mass-like regulators the

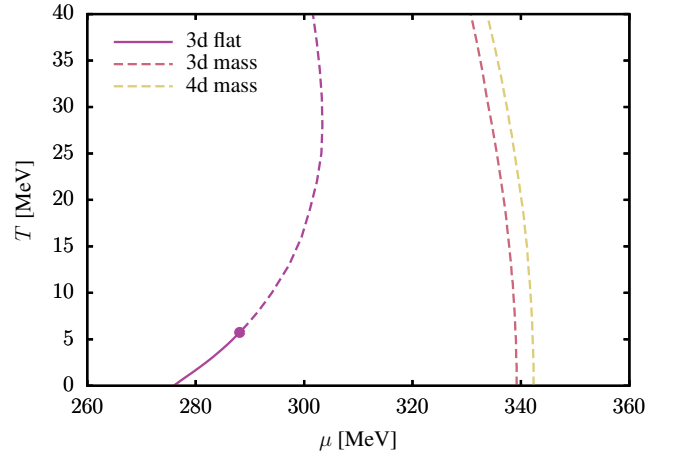


Figure 2. Regulator scheme dependence of the chiral transition for three different regulators. Line styles similar to Fig. 1.

chiral transition is a smooth crossover and the critical endpoint which is still present at  $T \approx 6$  MeV for the flat regulator is gone (basically pushed below the  $\mu$ -axis); this behavior should not be over-interpreted since the location of the critical endpoint strongly depends on parameter choices [58]. Both crossovers are closely aligned at  $T = 0$ :  $\mu^{(\text{cross}, 3\text{d})} \approx 339$  MeV and  $\mu^{(\text{cross}, 4\text{d})} \approx 342$  MeV, respectively. The difference of about 3 MeV is not of significance since no particular fine-tuning of the starting parameters for the chiral condensates has been taken into account. Since there are no qualitative differences between the two crossovers it seems that dimensionally reduced regulators are an appropriate choice for the analysis of finite- $\mu$  thermodynamics.

In the chiral limit when the explicit symmetry breaking term  $c$  in the action vanishes, a first-order phase transition for both mass-like regulators is found. The critical chemical potential is smaller but always above the vacuum quark mass in this case. Interestingly, this is in accordance with a similar work [47] where a different exponential regulator was employed for the bosonic fluctuations. Contrarily, with the 3d flat regulator the phase transition at vanishing temperature is always of first-order regardless of the explicit symmetry breaking and the critical chemical potential is smaller than the vacuum quark mass.

Characteristic for the back-bending is the occurrence of a negative entropy density  $s$  beyond the chiral transition line at small temperatures. As already discussed in [24] the back-bending is in agreement with the Clausius-Clapeyron relation

$$\frac{dT_c}{d\mu_c} = -\frac{\Delta n}{\Delta s}, \quad (29)$$

since a positive particle density difference  $\Delta n$  and a negative entropy density difference  $\Delta s$  result in a finite positive slope of the (first-order) transition line on the  $\mu$ -axis. A comparison of the thermodynamics is given in Fig. 3 where the entropy density in the low-temperature region of the phase diagram for the two 3d regulators is shown. The left panel

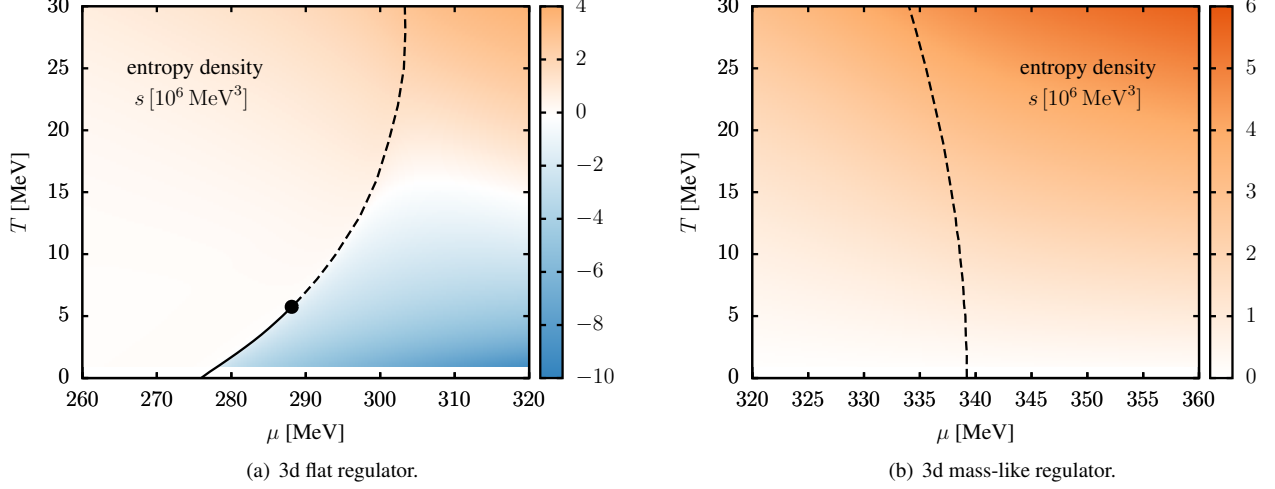


Figure 3. Entropy density for the 3d flat (left panel) and 3d mass-like (right panel) regulators close to the zero-temperature chiral phase boundary. The lower blue-shaded region denotes a negative entropy density.

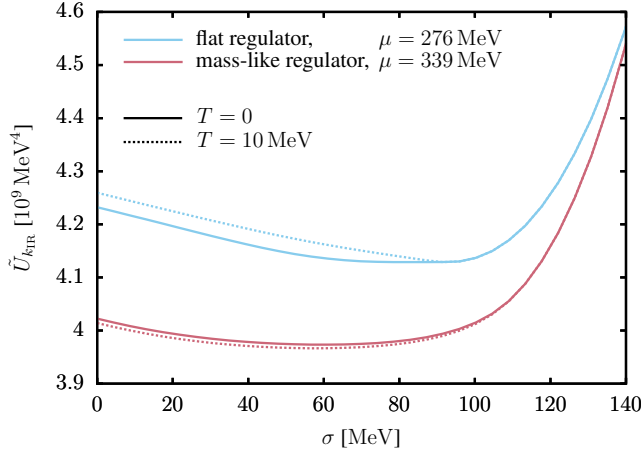


Figure 4. 3d flat and 3d mass-like effective potentials with explicit symmetry breaking at  $k_{\text{IR}} = 50$  MeV for  $T = 0$  (solid) and  $T = 10$  MeV (dotted) as a function of the radial  $\sigma$ -mode. The chemical potential is fixed to the respective zero-temperature transitions:  $\mu_c^{(1\text{st-order})} \approx 276$  MeV for the flat and  $\mu_c^{(\text{cross})} \approx 339$  MeV for the mass-like regulator. The mass-like regulator potential has been shifted by a constant for comparison.

shows the expected negative entropy density (blue shaded region) for the flat regulator [24]. With the mass-like regulator (right panel) the negative entropy density vanishes along with the back-bending.

The notably different back-bending behavior between the 3d flat and the 3d mass-like regulators is also visible in the fully evolved effective potential. In Fig. 4 both effective potentials  $\tilde{U}_{k_{\text{IR}}} \equiv U_{k_{\text{IR}}} - c\sigma$ , i.e., with an explicit symmetry breaking term and evolved to  $k_{\text{IR}} = 50$  MeV, are shown as a function of the radial  $\sigma$ -mode for temperatures  $T = 0$  (solid lines) and  $T = 10$  MeV (dotted lines). The corresponding chemical potentials are each fixed close to the transition at

vanishing temperature: for the flat regulator  $\mu_c^{(1\text{st-order})} \approx 276$  MeV (blue colors) and for the 3d mass-like regulator  $\mu_c^{(\text{cross})} \approx 339$  MeV (red colors) where the latter potential has been shifted by an irrelevant constant for a better comparison. One sees that the infrared potential for the mass-like regulator decreases for increasing temperature while the opposite behavior is found for the 3d flat regulator where the potential increases with increasing temperature. This in turn means that there is stronger spontaneous chiral symmetry breaking for the flat regulator since the potential minimum is pushed to larger values for increasing temperature. This causes the back-bending of the transition line. For the mass-like regulator the potential minimum decreases slightly with increasing temperature such that the chiral transition shifts to smaller chemical potentials and thus no back-bending occurs.

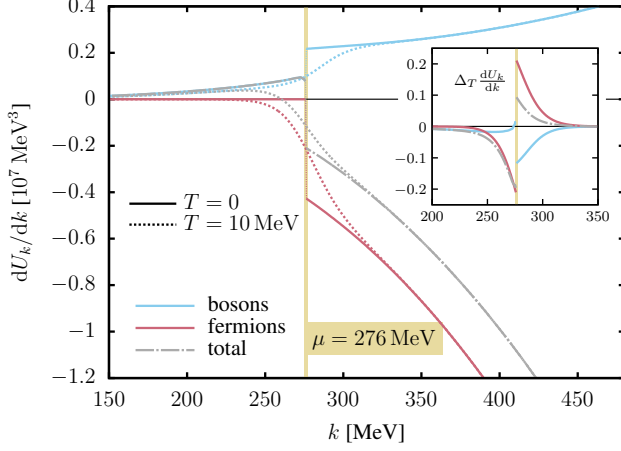
This different temperature progression of the potentials can be further traced back to a different flow behavior of the fermion contributions which contain the explicit  $\mu$ -dependence. At small temperatures and for increasing chemical potential, the thermodynamic contributions progressively cancel out the vacuum flow, generally leading to a decoupling behavior of the fermions.

For the 3d mass-like regulator the zero-temperature fermionic flow, Eqs. (22) and (20), can be rewritten as

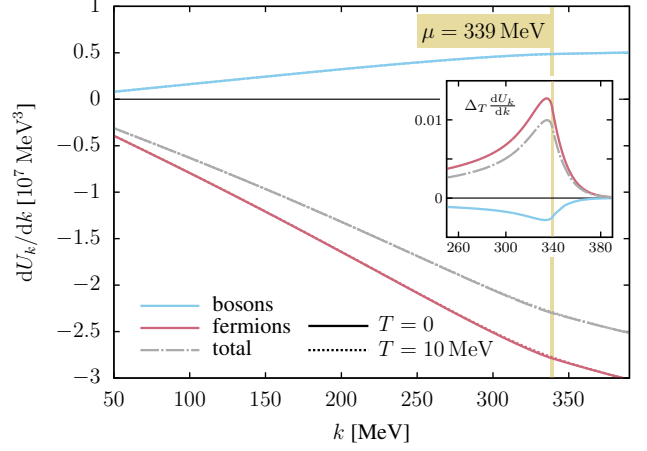
$$\partial_t U_k^{F,\text{mass}} = -\frac{\nu k^2}{4\pi^2} \int_{p_F}^{k_\phi} d|p| \frac{p^2}{E_\psi} \quad (30)$$

with the quark energy  $E_\psi = \sqrt{p^2 + m_{\text{eff},\psi}^2}$ . Due to the regulator's momentum independence, the quark energy  $E_\psi$  looks like an ideal or free dispersion relation depending on the spatial momenta with an effective scale-dependent quark mass  $m_{\text{eff},\psi} = \sqrt{k^2 + m_\psi^2}$ . The lower boundary of the momentum





(a) 3d flat regulator.



(b) 3d mass-like regulator.

Figure 5. Contributions to the potential flow for  $T = 0$  (solid and dash-dotted) and  $T = 10$  MeV (dotted) at  $\sigma = 0$  as a function of the RG scale  $k$ . Left: 3d flat regulator; right: 3d mass-like regulator. The inlay shows the respective  $T = 0$  flows subtracted from the  $T = 10$  MeV flows. Chemical potentials (vertical lines) are chosen as in Fig. 4.

integration defines a Fermi momentum

$$p_F := \begin{cases} \sqrt{\mu^2 - m_{\text{eff},\psi}^2}, & \mu > m_{\text{eff},\psi} \\ 0, & \text{else} \end{cases} \quad (31)$$

For  $\mu > m_\psi$  (not  $m_{\text{eff},\psi}$ ) and  $k$  sufficiently small, the momentum space in the integral is gradually suppressed by occupied quark states below the Fermi surface and the fermions decouple from the flow. In other words, the chemical potential serves as an effective infrared cutoff.

This is in contrast to the flat regulator where the decoupling is not gradual but occurs at a sharp RG scale  $k_F$ . For this regulator the fermionic flow, Eqs. (23) and (24), is a sharp step function at vanishing temperature

$$\partial_t U_k^{F,\text{flat}} = -\frac{\nu k^5}{12\pi^2} \Theta(E_\psi - \mu) \quad (32)$$

with energies  $E_\psi = \sqrt{k^2 + m_\psi^2}$  which do not depend on spatial momenta. Here, for  $\mu > m_\psi$ , the flow discontinuously jumps to zero at  $k_F = \sqrt{\mu^2 - m_\psi^2}$ .

A visualization of the flow around the Fermi surface is given in Fig. 5, on the left for the 3d flat regulator and on the right for the 3d mass-like regulator. In each panel three different flows evaluated at  $\sigma = 0$  are shown as a function of the RG scale. The total flow  $\partial_k U_k$  (gray lines) assembles the bosonic (blue upper lines) and fermionic (red lower lines) flows. Solid and dash-dotted lines are the flows at zero temperature and the dashed lines the ones for  $T = 10$  MeV. The 3d flat regulator (left) induces via the  $\Theta$ -function a discontinuous jump at  $T = 0$  in all three flows at the critical chemical potential. The fermionic flow jumps to zero at  $k_F = \mu$  since the quark mass  $m_\psi$  vanishes for  $\sigma = 0$ . Consequently, the total flow changes sign and is given completely by the bosonic contribution that tries to restore chiral symmetry. This behavior is smeared out

at finite temperatures and the contribution of the bosons weakens overall. As a net effect chiral symmetry breaking becomes stronger at finite temperatures which finally yields the back-bending of the transition line in the phase diagram.

In the inlays of both panels of Fig. 5 the temperature difference  $\Delta_T(dU_k/dk)$  of the zero temperature flow subtracted from the  $T = 10$  MeV flow is displayed for the same three potential contributions (same linestyle is used). For the flat regulator (left inlay) an expected discontinuity arises at the Fermi surface and the sign of the enclosed area of the fermionic flow difference and hence total flow contribution changes. Since the areas of the fermionic flow are almost of the same magnitude around the critical chemical potential the fermionic flow decouples from the further evolution towards the infrared. The consequence is that the net total flow is dominated by the asymmetric bosonic contributions. Their difference is negative everywhere and pushes the potential contribution to larger values which finally drives the chiral symmetry breaking.

This behavior is in contrast to the one with a 3d mass-like regulator (right panel) where a smooth decoupling takes place around the corresponding smooth transition. The total flow stays negative and is almost insensitive to small temperature variations, which in turn produces the perpendicular evolution of the smooth transition line in the phase diagram.

Similarly, in the right inlay of Fig. 5 no sharp decoupling of the fermionic flow around the Fermi surface is found. The flow differences peak close to the Fermi scale  $k_F$  but contribute to the total flow for all scales (despite the different order of magnitudes in the inlays). Since the difference in the total flow stays positive at all scales no back-bending is found.

Noteworthy, the back-bending phenomenon does not only occur for a strict discontinuity in the fermion flow. For any other tested regulator back-bending can be observed as soon as the fermionic flow contribution decouples completely (tends to zero) from the total flow at a finite scale  $k > 0$ , albeit the back-coupling seems to be stronger the more rapidly the

decoupling happens.

In summary, the choice of the regulator function has a crucial influence on the momentum structure of the loop integrals of the flow equations. Thus, an incongruous choice can potentially cause unphysical regulator effects. An extreme example is given by the discussed flat regulator in LPA which, albeit optimized in the vacuum, cancels all momentum dependence of the propagator. As demonstrated above this leads at finite chemical potential to a back-bending and negative entropy density beyond the chiral transition. The mass-like regulator does not modify the momentum structure at all and leads to a smooth Callan-Symanzik type flow which does not produce such regulator artifacts.

The Wetterich equation explicitly allows for an arbitrary choice of regulator functions that fulfill the criteria summarized in Sec. III, see also App. A. The flow equation in LPA, however, keeps the momentum structure of the two-point function  $\Gamma_k^{(2)}(p) = p^2 + m_k^2$  generically fixed such that the flow cannot compensate for the particular choice of momentum dependence for  $R_k(p^2)$ . Consequently, contributions which are sensitive to the momentum structure, as for example the fermion decoupling discussed above, can lead to a strong scheme dependency.

However, for more involved truncations where for example generally momentum dependent wave function renormalization  $Z_k(p)$  are taken into account such regulator effects are not expected to appear anymore.

## VI. Summary and Conclusions

The functional renormalization group method is a powerful non-perturbative tool that has a broad variety of research fields. A key ingredient of the flow equation is the regulator that suppresses the infrared physics via an infrared cutoff. The optimal choice of the regulator function plays a major role in the quantitative optimization of actual calculations. Recently, great improvements could be achieved by the application of the principle of minimum sensitivity within  $O(N)$ -models which demonstrate the convergences of the derivative expansion to accurate and precise results [37].

In addition to a suitable choice of the regulator, any functional equation must be truncated for technical reasons in general to obtain a finite system of equations that allows a numerical treatment. Feasible truncations in QCD applications are often more limited than in simpler model studies such that one relies on more general optimization criteria [30, 59]. In particular, the impact of a finite chemical potential on possible truncation errors is essentially unknown. Especially, at low temperatures and finite density, strange effects like the observed back-bending of the chiral transition line in various low-energy effective models [23, 25] and the associated occurrence of negative entropy densities beyond the transition [24] could hint at the existence of large truncation artifacts.

The focus of this work is the regulator scheme dependence of functional renormalization group equations at finite density. General considerations on a reasonable choice of regulator including convergence properties in particular at finite density

are given and confronted to various known optimization criteria in the literature. As an application the chiral phase structure of the quark-meson model at low temperatures has been calculated with three different regulators in local potential approximation. Within this approximation we have found clear evidence that the back-bending of the transition line and the odd appearance of a negative entropy density are related to the choice of the regulator function.

For momentum-independent Callan-Symanzik type regulators the chiral phase transition is a smooth crossover for physical pion masses and the transition line hits the  $\mu$ -axis perpendicularly. No negative entropy densities are observed in contrast to the familiar back-bending scenario with the optimized flat regulator.

This essentially allows for two different interpretations: firstly, the Callan-Symanzik regulator, which seems to be an sub-optimal regulator in critical exponents evaluations [52], is just incapable of resolving some of the physical intricacies leading thus to the back-bending phenomenon in the phase structure, or secondly, the back-bending is an actual unphysical artifact induced by the nontrivial momentum structure of the flat regulator in local potential approximation.

A detailed investigation of the renormalization group flow reveals that the back-bending is induced at scales around the Fermi surface. For the flat regulator, it appears as a discontinuity in the fermion flow that is smeared out at finite temperature. This smearing feeds back into the bosonic flow and leads to a large temperature sensitivity which can eventually be observed in the curvature of the transition line. For Callan-Symanzik type regulators, the Fermi distributions are fully integrated out in the Wetterich loops and therefore lead only to small, thermodynamically sensible modifications. Moreover, at the level of the LPA the momentum structure of the loop integral is fully determined by the choice of regulator function because higher orders of momenta, such as of  $\mathcal{O}(p^4)$ , are neglected in the effective action. In total, these findings lead to the conclusion that the back-bending phenomenon found in local potential approximation is a non-physical artefact induced by the specific choice of the shape function.

We remark that the absence of the above mentioned truncation artifacts for Callan-Symanzik regulators does not imply a full and sufficient convergence meaning that the obtained results could still be quite insufficient from a more quantitative viewpoint. One idea to circumvent this possible constraint is the simultaneous combination of regulator functions such that the accuracy can be improved and additionally avoids the back-bending issue. Of course, when no truncation is made at all, a full solution for the effective average action does not depend on the choice of regulator, whereas any sort of truncations introduces a spurious dependence on it. On a more advanced level, by going beyond the LPA a more complex momentum structure of the effective action might remedy the problem regardless of the regulator function. For example we expect that the inclusion of higher momentum-dependent wavefunction renormalizations will certainly affect such regulator effects but it is still an open issue how large the truncation artifacts of higher truncation orders are.

## Acknowledgments

We thank Jan Pawłowski and Fabian Rennecke for interesting and enlightening discussions. We acknowledge support by the Helmholtz Graduate School for Hadron and Ion Research for FAIR, the GSI Helmholtzzentrum für Schwerionenforschung and the BMBF under Contract No. 05P18RGFCA. KO acknowledges funding by the German Academic Scholarship Foundation and BJS by the Deutsche Forschungsgemeinschaft (DFG) through the grant CRC-TR 211 “Strong-interaction matter under extreme conditions”.

### A. General Optimization Criteria

Finding an *optimal* shape function  $r(y)$  in the sense that the truncation error is minimized, i.e., that for a given set of observables  $\{O_n\}$  their physical values are approached as closely as possible, is a non-trivial task. So far, three different criteria are found in the literature of which a brief summary shall be given in this appendix.

The principle of minimum sensitivity (PMS) [60], first applied in perturbation theory, aims at finding solutions that are least sensitive to variations in the regularization scheme. In practice, this usually entails a full computation of the RG flow of the given set of observables  $\{O_n\}$  under variation of one or more parameters of a parameterized shape function. A coinciding extremum for all  $O_n$  is searched for. However, such calculations are computationally expensive and solutions are not necessarily unique or exist at all, see e.g. [30] for a discussion. However, despite those drawbacks this criterion has been successfully applied in the past to, for example, the accurate determination of critical exponents of the three-dimensional Ising model [38, 61]. Recently, successive improvements have been made with the application of the PMS to fix the regulator dependence which establishes the convergence of the derivative expansion with great precision and accuracy [37, 62].

An observable-independent criterion that provides very precise values for critical exponents [52] has been put forward in [59]. It is based on the idea that regulators which maximize the gap in the massless inverse dimensionless propagator  $P^2(y)$ , Eq. (5), yield the greatest stability of the flow and the quickest approach towards the physics in the IR:

$$C_{\text{opt}} := \max_R \left( \min_{y \geq 0} P^2(y) \right). \quad (\text{A1})$$

One reasoning for this assumption is that for the largest gap an expansion of the flow in inverse powers of  $P^2$  leads to a most rapid convergence of the series, see [63] for further details. All regulators that fulfill Eq. (A1), further need to obey a normalization condition since otherwise  $C_{\text{opt}}$  could be made arbitrarily large. The usual choice is to set

$$R_k(y_0 k^2) = y_0 k^2 \quad (\text{A2})$$

or, equivalently, to fix  $r(y_0) = 1$  for some positive  $y_0 > 0$

[59]. A more general form  $r(y_0) = c$  with any finite positive  $c > 0$  is also possible [30].

To ensure that  $y_0$  exists and is unique, we restrict ourselves to continuous, strictly monotonously decreasing shape functions  $r(y)$  in the following. This kind of normalization is closely related to the introduction of an effective RG scale  $k_{\text{eff}}$ : for a given  $r(y)$  with normalization  $r(y_0) = 1$  one can define a family of shape functions

$$r^\lambda(y) := r(y/\lambda^2) \quad (\text{A3})$$

where  $r^\lambda$  is obtained from the original shape function  $r$  by a rescaling  $k \rightarrow \lambda k$  with  $\lambda > 0$ . Clearly, this shift in the effective RG scale leads to the same trajectory in theory space, corresponding just to a different parameterization of the effective action  $\Gamma_k^\lambda \equiv \Gamma_{\lambda k}$  where  $\Gamma^\lambda$  is the effective action obtained with  $r^\lambda$ . If we now set  $k_{\text{eff}}^2 := y_0 k^2$ , the rescaling shifts  $k_{\text{eff}} \rightarrow \lambda k_{\text{eff}}$  and  $r^\lambda$  obtains a different normalization  $r^\lambda(\lambda^2 y_0) = 1$ . Hence, for monotonous shape functions the normalization singles out exactly one regulator from each family of equivalent regulators that differ only by a constant multiplicative shift in  $k_{\text{eff}}$ . The optimization criterion Eq. (A1) thus only compares regulators with the same  $k_{\text{eff}}$  which depends on  $k$ , i.e.  $k_{\text{eff}}(k)$ . The optimal gap is attained when  $P^2(y)$  has its minimum at  $y_0$ . With the normalization  $r(y_0) = 1$  in Eq. (5) the optimal gap in LPA and for vanishing fields is thus  $C_{\text{opt}} = 2y_0$  according to this criterion [64].

A popular choice of an optimal regulator is the flat (or Litim) regulator [64]

$$r_{\text{flat}}(y) = \left( \frac{1}{y} - 1 \right) \Theta(1 - y). \quad (\text{A4})$$

This is not the unique solution to Eq. (A1). Many more regulator shape functions that fulfill the optimization criterion can be found in the literature. Oftentimes, they can be obtained from generalized regulator classes like the compactly supported smooth (CSS) regulators [65]. However, the flat regulator (A4) is special in the sense that the shape function is optimal for *any* arbitrary normalization point  $c$ , i.e.,  $r(y_0) = c$  with  $y_0 = 1/(c + 1)$ .

The special role of the flat regulator in LPA is further confirmed by a third functional optimization criterion developed in [30, 66]. It is also grounded on a stability assumption for correlation functions that should be insensitive to local variations of the regulator at a fixed physical cutoff scale  $k_{\text{phys}}$ . The physical cutoff scale  $k_{\text{phys}}$  is here given by the gap of the inverse propagator.

The condition can be related to the minimization of the kernel of the flow operator  $\partial_t$  that minimizes the total length of the flow trajectory in the theory space, see [66] for further details. In LPA and for a single scalar field the criterion reduces to a bounded dimensionless shape function for all momenta,

$$r_{\text{opt}}(y) \leq r, \quad \forall r, y, \quad (\text{A5})$$

with the normalization condition

$$\min_{y \geq 0} P^2(y) = k_{\text{phys}}^2/k^2. \quad (\text{A6})$$

In contrast to the previous criterion Eq. (A1) where the gap is maximized for shape functions intersecting at a common point, this criterion compares regulators leading to the same gap and chooses the one that maximizes the propagator over the whole spectrum. For the *special* choice  $k_{\text{phys}} = k$ , the flat regulator is the unique solution to the criterion Eq. (A5).

We close this recapitulation of optimization criteria with two remarks: the mentioned optimization criteria do not change when the truncation of the effective action is improved beyond LPA by taking momentum-independent wave function renormalization  $Z_k$  into account, often denoted as LPA' in the literature. For example, augmenting Eq. (4) with the wave-function renormalization,

$$R_k(p^2) = Z_k p^2 r(y), \quad (\text{A7})$$

implies the propagator modification  $P^2 \rightarrow Z_k P^2$  and allows for a systematic inclusion of higher derivative operators in Eq. (2).

Secondly, the previous arguments and criteria can be straightforwardly adapted to fermions. To preserve, e.g., chiral and gauge symmetries, a regulator resembling a kinetic term, cf. Eq. (4), can be chosen as

$$R_k^F(p) = Z_k i \not{p} r^F(y). \quad (\text{A8})$$

The fermionic analogon to Eq. (5) (for  $Z_k = 1$ ) follows from the inverse propagator [64]

$$P_F^2(y) = y[1 + r^F(y)]^2, \quad (\text{A9})$$

such that the choice

$$r^F(y) = \sqrt{1 + r(y)} - 1 \quad (\text{A10})$$

leads to the same effective regulator scheme. This yields the fermionic version of the flat regulator shape function

$$r_{\text{flat}}^F(y) = \left( \sqrt{\frac{1}{y}} - 1 \right) \Theta(1 - y). \quad (\text{A11})$$

## B. Approximate Flows in the Chirally Symmetric Regime

In [56] it was observed that the two-flavor quark-meson model exhibits an approximate partial IR fixed point behavior in the chirally symmetric regime. This can be taken advantage of to constrain the effective potential at the chiral symmetry breaking scale  $k_\chi$ . We detail here the technical derivation of the fixed point values used in Sec. IV B in a general, regulator-independent way. This follows closely the arguments made in [56] but generalizes them to regulators that incorporate an additional scale, such as the mass-like regulators Eq. (15) and Eq. (16) which depend on  $k_\phi$ . The chain of argument relies on the consideration of vacuum flows in LPA', i.e., with running wavefunction renormalizations and a running Yukawa coupling. At large RG scales  $k > k_\chi$ , fluctuations are dominated by the purely fermionic contributions. Picking up the

definitions for  $\tilde{\rho}$  and  $u_k(\tilde{\rho})$ , Eq. (26) and Eq. (25), the approximate flow of the dimensionless potential at fixed  $\tilde{\rho}$  becomes

$$\partial_t u_t(\tilde{\rho}) = -4u_t + (2 + \eta_{\phi,t}) \tilde{\rho} u_t'(\tilde{\rho}) - \frac{N_c N_f}{4\pi^2} l_{0,t}^F(\tilde{m}_{\psi,t}^2). \quad (\text{B1})$$

To simplify the notation in the upcoming discussion, an explicit scale dependence is now expressed by the RG time  $t = \ln(k/k_\phi)$  instead of the corresponding dimensionful scale  $k$  in the lower index. The fermion loop is expressed in terms of the threshold function which reads for 4d regulators

$$l_{0,t}^{F,4d}(\tilde{m}_{\psi,t}^2) = \int_0^\infty dy y^2 \frac{[1 + r_t^F(y)] \partial_t r_t^F(y)}{y [1 + r_t^F(y)]^2 + \tilde{m}_{\psi,t}^2} \quad (\text{B2})$$

and for 3d regulators

$$l_{0,t}^{F,3d}(\tilde{m}_{\psi,t}^2) = 2 \int_0^\infty dx x^{3/2} \frac{[1 + r_t^F(x)] \partial_t r_t^F(x)}{\sqrt{x [1 + r_t^F(x)]^2 + \tilde{m}_{\psi,t}^2}}. \quad (\text{B3})$$

The dimensionless quark mass is given by

$$\tilde{m}_{\psi,t}^2 = \frac{\bar{g}_t^2}{2} \tilde{\rho}. \quad (\text{B4})$$

Note the factors in the definitions of the threshold functions have been chosen in agreement with [56] for better comparability. We allow for an explicit scale dependence of  $r_t^F$  beyond that of its argument  $y = p^2/k^2$  or  $x = \mathbf{p}^2/k^2$ , as denoted by the index  $t$ . Such a dependence exists, for example, for the mass-like regulators via the dimensionless UV scale  $\tilde{k}_\phi := k_\phi/k = e^{-t}$ . If the shape function does not possess an explicit scale dependence, the threshold functions  $l_{n,t}^F(\tilde{m}_{\psi,t}^2)$  only depend on  $t$  implicitly via the quark-mass argument. By definition, the higher-order threshold functions  $l_{n,t}^F$  are related to  $l_{0,t}^F$  via [56]

$$l_{n,t}^F(\tilde{m}_{\psi,t}^2) := \frac{(-1)^n}{(n-1)!} \left( \frac{d}{d\tilde{m}_{\psi,t}^2} \right)^n l_{0,t}^F(\tilde{m}_{\psi,t}^2). \quad (\text{B5})$$

The quark anomalous dimension generally vanishes in this approximation and the meson anomalous dimension can be written

$$\eta_{\phi,t} = \frac{N_c N_f}{16\pi^2} \bar{g}_t^2 \kappa_t^F. \quad (\text{B6})$$

$\kappa_t^F$  denotes the purely fermionic part of the corresponding threshold function evaluated at  $\tilde{\rho} = 0$ . We do not give an explicit expression as it is not required. The flow of the Yukawa coupling is solely fed by its renormalization,

$$\partial_t \bar{g}_t^2 = \eta_{\phi,t} \bar{g}_t^2, \quad (\text{B7})$$

and has the solution

$$\bar{g}_t^2 = \frac{\bar{g}_0^2}{1 - \frac{N_c N_f}{16\pi^2} \bar{g}_0^2 \int_0^t ds \kappa_s^F} \quad (\text{B8})$$



where  $g_0$  is the initial value at  $t = 0$ . Expanding  $u_t(\bar{\rho})$  in a power series, see Eq. (27), flow equations for the coefficients  $u_t^{(n)}(0)$  can be inferred from Eq. (B1) and similar exact solutions. For  $n = 2$ , one finds

$$\frac{u_t^{(2)}(0)}{\bar{g}_t^2} = \frac{\frac{u_0^{(2)}(0)}{\bar{g}_0^2} - \frac{N_c N_f}{16\pi^2} \bar{g}_0^2 \int_0^t ds l_{2,s}^F(0)}{1 - \frac{N_c N_f}{16\pi^2} \bar{g}_0^2 \int_0^t ds \kappa_s^F}. \quad (\text{B9})$$

Note that for any regulator shape function  $r^F$  without explicit  $t$  dependence, one obtains the simple relations  $\kappa^F = l_2^F(0) \equiv 1$  [56]. In this case, the solution simplifies to

$$\frac{u_t^{(2)}(0)}{\bar{g}_t^2} = 1 - \frac{1 - \frac{u_0^{(2)}(0)}{\bar{g}_0^2}}{1 - \frac{N_c N_f}{16\pi^2} \bar{g}_0^2 t} \quad (\text{B10})$$

and for  $t \rightarrow -\infty$  approaches the infrared fixed point

$$\left. \frac{u_t^{(2)}(0)}{\bar{g}_t^2} \right|_* = 1. \quad (\text{B11})$$

For the two mass-like regulators, the same infrared value is approached even though they require the more complex solution Eq. (B9): At large negative RG times  $t$ , the UV cutoff parameter  $\tilde{k}_\phi = e^{-t}$  diverges quickly and both  $\kappa_t^F$  and  $l_{2,t}^F(0)$  become effectively scale-independent, tending to unity. Thus, the leading contributions to the integrals in Eq. (B9) behave like  $t$  and all subleading terms vanish for  $t \rightarrow -\infty$ . A similar analysis works at all orders  $n \geq 3$  where the solution for the expansion coefficients reads

$$\begin{aligned} \frac{u_t^{(n)}(0)}{\bar{g}_t^{2n}} &= e^{2(n-2)t} \frac{u_0^{(n)}(0)}{\bar{g}_0^{2n}} - \frac{N_c N_f}{4\pi^2} \frac{(-1)^n (n-1)!}{2^n} \times \\ &\times e^{2(n-2)t} \int_0^t ds l_{n,s}^F(0) e^{-2(n-2)s}. \end{aligned} \quad (\text{B12})$$

In the case of scale-independent threshold functions  $l_n^F(0)$ , the integral can be solved trivially and the infrared fixed point is given by

$$\left. \frac{u_t^{(n)}(0)}{\bar{g}_t^{2n}} \right|_* = \frac{N_c N_f}{8\pi^2} \frac{(-1)^n (n-1)!}{2^n (n-2)} l_n^F(0). \quad (\text{B13})$$

At these orders of the expansion, the threshold functions depend on the explicit choice of shape function, i.e., they yield different fixed points for different regulators. From similar arguments as above, it follows that the infrared-attractive points for the mass-like regulators are determined by inserting the asymptotic threshold functions  $l_{n,t \rightarrow -\infty}^F(0)$  for  $l_n^F(0)$  in Eq. (B13).

### C. Pole Proximity of Vacuum Flows

In general, the non-perturbative flow equations are composed of threshold functions that accommodate prospective

singularities governed by the sign of the potential derivatives. A typical phenomenon occurs for vacuum flows of quark-meson model truncations (or similar theories) in LPA on a discretized  $\sigma$ -field grid: for small  $\sigma$ -values the pion threshold function is the dominant one in the IR and the pion mass  $m_\pi^2 = 2U'_k(\sigma^2)$  becomes negative in the vicinity of the pole in the (Euclidean) propagator. During the remaining IR evolution it follows closely along this regulator-dependent pole. This poses a significant numerical challenge since small numerical deviations can easily hit this pole.

In this appendix we estimate the proximity of the pion pole analytically as follows: The effective inverse pion propagator in LPA

$$\Gamma_{\pi,k}^{(2)}(p^2) + R_k(p^2) = k^2 P^2(p^2/k^2) + m_\pi^2, \quad (\text{C1})$$

exhibits a pole in the momenta as soon as  $m_\pi^2$  falls below a certain negative threshold (assuming the positivity of the inverse propagator  $P^2$ , Eq. (5)). The threshold is determined by the negative of the massless propagator gap

$$m_{\pi,\text{thres}}^2 = -k^2 \min_{y \geq 0} P^2(y). \quad (\text{C2})$$

This argument can straightforwardly be transferred to dimensionally reduced regulators. For a 3d regulator the two-point function reads accordingly

$$\Gamma_{\pi,k}^{(2)}(p_0, \mathbf{p}^2) + R_k(\mathbf{p}^2) = p_0^2 + k^2 P^2(\mathbf{p}^2/k^2) + m_\pi^2, \quad (\text{C3})$$

such that the threshold value at the minimal  $p_0^2 = 0$  is still given by Eq. (C2).

For a 3d flat regulator the minimum of the massless inverse propagator is at  $P^2(x) = 1$  and the pole for vanishing  $\sigma$ -field is located at  $U'_k = -k^2/2$ , cf. Eq. (23). For the dimensionless variable  $\tilde{u}'_k := 2U'_k/k^2$  the pion propagator pole is shifted to  $\tilde{u}'_k = -1$  with the corresponding flow equation evaluated at  $\sigma = 0$

$$\begin{aligned} \partial_t \tilde{u}'_k &= 2(\partial_t U'_k)/k^2 - 2\tilde{u}'_k \\ &= \frac{1}{\pi^2} \left[ -\frac{U''_k}{(1 + \tilde{u}'_k)^{3/2}} + \frac{\nu}{12} \left(\frac{g}{2}\right)^2 \right] - 2\tilde{u}'_k. \end{aligned} \quad (\text{C4})$$

A similar analysis for the 3d mass-like regulator, cf. Eq. (22), yields the flow equation (again evaluated at  $\sigma = 0$ )

$$\begin{aligned} \partial_t \tilde{u}'_k &= \frac{3U''_k}{\pi^2} \left[ \frac{\tilde{k}_\phi}{\sqrt{\tilde{k}_\phi^2 + 1 + \tilde{u}'_k}} - \text{artanh} \left( \frac{\tilde{k}_\phi}{\sqrt{\tilde{k}_\phi^2 + 1 + \tilde{u}'_k}} \right) \right] \\ &\quad - \frac{\nu}{4\pi^2} \left(\frac{g}{2}\right)^2 \left[ \frac{\tilde{k}_\phi}{\sqrt{\tilde{k}_\phi^2 + 1}} - \text{artanh} \left( \frac{\tilde{k}_\phi}{\sqrt{\tilde{k}_\phi^2 + 1}} \right) \right] - 2\tilde{u}'_k \end{aligned} \quad (\text{C5})$$

that additionally depends on the dimensionless parameter  $\tilde{k}_\phi := k_\phi/k \geq 1$  which increases during the IR evolution.

Both equations are displayed in Fig. 6 where the flows  $\partial_t \tilde{u}'_k$  are given as a function of  $\tilde{u}'_k$  for four different  $U''_k = (-1, 0, 1, 22.6)$  (from top to bottom). The solid orange lines

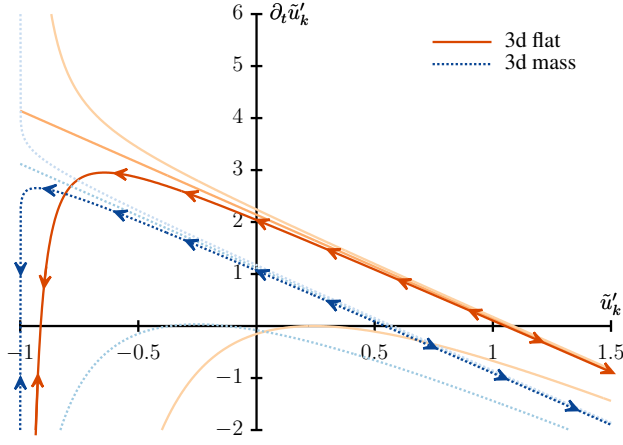


Figure 6. Flow of  $\tilde{u}'_k$  evaluated at  $\sigma = 0$  for the two 3d regulators, cf. Eqs. (C4) and (C5).  $U''_k = (-1, 0, 1, 22.6)$  (from top to bottom) and  $\tilde{k}_\phi = 1$  for the mass-like regulator.

are the results for the 3d flat regulator and the dashed blue lines for the 3d mass-like regulator (for  $\tilde{k}_\phi = 1$ ). The parameters in both quark flow contributions are kept fixed to  $g = 6.5$  and  $\nu = 24$ .

Generically, the structure of the flow equation for all discussed regulators is very similar at  $\sigma = 0$ : For  $U''_k > 0$  but below a certain positive value  $U''_{k^*}$  two stationary points defined by  $\partial_t \tilde{u}'_k = 0$  appear and for  $U''_k < 0$  only one stationary point (in the figure: the one on the right side where  $\tilde{u}'_k > 0$ ) survives. Note that these points are not actually fixed points since their location depends on  $U''_k$  and changes during the flow. For increasing  $U''_k$  both stationary points come closer to each other and degenerate at  $U''_{k^*}$  ( $U''_{k^*} \sim 22.6$  for the 3d flat regulator and  $U''_{k^*} \sim 23.1$  for the 3d mass-like regulator). For larger values they disappear completely.

Since the flow equations are integrated in negative  $t$ -direction,  $\tilde{u}'_k$  increases for  $\partial_t \tilde{u}'_k < 0$  and decreases for  $\partial_t \tilde{u}'_k > 0$ . As a consequence, the right stationary point is a repulsive point (it has a negative slope) while the left point in the vicinity of the pole is an attractive one with a positive slope. The flow pattern of two exemplary curves are indicated by arrows in Fig. 6.

Therefore, for  $U''_k \in ]0, U''_{k^*}[$  and for values of  $\tilde{u}'_k$  smaller than the repulsive point, the derivative is always pushed towards the attractive left point and thus never runs into the pole. It might be that the flow oscillates around this attractive point towards the IR which would aggravate its numerical treatment. For a negative  $U''_k$  only the right repulsive point exists in the flow pattern but this case would lead to a flow directly into the pole for  $\tilde{u}'_k$  values smaller than this point. For  $\tilde{u}'_k$  values larger than the repulsive point a permanent flow towards increasingly positive values emerges. Similar, for sufficiently large  $U''_k > U''_{k^*}$  no stationary points exist anymore and the flow is always driven to positive values, avoiding a chiral symmetry breaking since  $\tilde{u}'_k$  becomes increasingly large.

Due to the convexity of the Wetterich flow equation the eventually IR evolved potential is also convex such that the

physical relevant case is the one where the second potential derivative  $U''_k$  tends to zero. This pushes, according to Eq. (C4), the stationary point around the pole even closer to it. In order to estimate the pole proximity we introduce the quantity  $\delta u$  through  $\tilde{u}'_k = -1 + \delta u$ . Multiplying both sides of Eq. (C4) with  $\delta u^{3/2}$  and setting  $\partial_t \tilde{u}'_k = 0$  we find to lowest order in  $\delta u$

$$\delta u \approx \left( \frac{U''_k}{2\pi^2 + \frac{\nu}{12} \left(\frac{g}{2}\right)^2} \right)^{2/3}. \quad (\text{C6})$$

For  $U''_k = 1$  this yields approximately  $\delta u \approx 0.0843$  and is in agreement with an error of less than 1% in the previous numerical calculated pole  $\tilde{u}'^{(0)}_k$ .

A similar treatment of the flow equation for the 3d mass-like regulator yields a comparable pole proximity. Explicitly, setting  $\partial_t \tilde{u}'_k = 0$ , the poles in Eq. (C5) can be eliminated by exponentiating again both sides with the result to lowest order

$$\delta u \approx 4\tilde{k}_\phi^2 \exp \left[ -2 - \frac{8\pi^2}{12U''_k} \left( \partial_t \tilde{u}'_k|_\psi + 2 \right) \right], \quad (\text{C7})$$

where  $\partial_t \tilde{u}'_k|_\psi$  is the  $U''_k$  independent (but  $k_\phi$  dependent) fermionic part of the flow for  $\tilde{u}'_k$ , see Eq. (C5).

Already for  $U''_k = 1$  and for  $\tilde{k}_\phi = 1$  one finds  $\delta u \approx 6.619 \times 10^{-10}$  being significantly closer to zero (and much smaller in comparison to the flat regulator proximity). This is nicely visible in Fig. 6.

A comparison of both estimates reveals that for the mass-like regulator the proper numerical treatment of the corresponding flow equations is much more involved. Furthermore, the estimate is further suppressed exponentially with decreasing  $U''_k$  compared to the power-law suppression for the flat regulator. However, the situation does not change significantly in the 4d regulator case. For completeness, the flow equation with a 4d mass-like regulator

$$\begin{aligned} \partial_t \tilde{u}'_k = & -\frac{3U''_k}{2\pi^2} \left[ -\frac{1}{1 + \frac{1+\tilde{u}'_k}{\tilde{k}_\phi^2}} + \ln \left( 1 + \frac{\tilde{k}_\phi^2}{1 + \tilde{u}'_k} \right) \right] \\ & + \frac{\nu}{8\pi^2} \left( \frac{g}{2} \right)^2 \left[ -\frac{1}{1 + \tilde{k}_\phi^{-2}} + \ln(1 + \tilde{k}_\phi^2) \right] - 2\tilde{u}'_k \end{aligned} \quad (\text{C8})$$

leads to the pole proximity

$$\delta u \approx \frac{\tilde{k}_\phi^2}{\exp \left[ \frac{2\pi^2}{3U''_k} \left( 2 + \partial_t \tilde{u}'_k|_\psi \right) + 1 \right] - 1} \quad (\text{C9})$$

that yields  $\delta u \approx 1.198 \times 10^{-8}$  for the same parameters.

Already in [59] it was shown that an optimized regulator according to the criterion Eq. (A1) pushes the propagator poles as far as possible down on the negative  $U''_k$ -axis and it was speculated that such regulators, in particular the flat regulator, thus lead to the smoothest and numerically most stable flow.

For the mass-like regulator, the pion pole proximity seems to be particularly grave as demonstrated in Fig. 6. A numerical solution for the vacuum flow, as argued above, is with standard methods not possible.

Note that in this work a numerical solution of this issue was not necessary due to the Silver Blaze property at  $T = 0$  and  $\mu \lesssim \mu_c$ . For this parameter regime the potential is only modified around small field values. Around the vacuum expectation value the potential remains unchanged and allows for a proper determination of the vacuum masses and condensate.

For future applications the analytical estimates for the stationary points in the flows might be an additional useful reference to stabilize the numerical setup

#### D. Numerical Implementation

In this appendix the numerical procedure for solving the flow equations in LPA is provided. Generally, a flow equation for the effective potential is a partial differential equation (PDE) for two independent variables  $t$  and  $\sigma$ . They feature a first-order derivative of the potential with respect to the logarithmic RG scale  $t = \ln k$  and a first- and second-order potential derivative with respect to the square of the radial  $\sigma$ -mode in field space, cf. Eq. (18), which turn them into coupled highly non-linear equations. Traditionally, these equations are solved on (equidistant) grids in the field variable  $\sigma$  or  $\sigma^2$ , with field derivatives obtained from finite differences, coupled Taylor-grid approximations [67], or cubic splines [68]. Global approaches with pseudo-spectral methods have also

been employed [69]. Recently, it has been shown that PDEs of the Wetterich equation-type in LPA can be recast into another shape: using the flow for the first potential derivative  $\partial_t U'_k$  a conservative form with distinct convective and diffusive fluxes can be constructed [28]. This admits a modern treatment within a hydrodynamic framework, utilizing finite volume methods [70] or more advanced setups like discontinuous Galerkin methods [27, 28]. Especially, shocks occurring in flows with a flat regulator caused by the discontinuity at the Fermi surface can be resolved in great detail within such a novel framework. Recently, in a first detailed study of the phase diagram of the quark-meson model with discontinuous Galerkin methods [27] the back-bending behavior of the chiral transition line at finite densities has also been observed which demonstrates that the back-bending is not an artefact of the numerical implementation to solve the flow equations. We therefore retain a more well-tried, computationally less expensive setup with a simpler implementation based on cubic splines over an equidistantly distributed grid in the  $\sigma$ -field space. The two missing boundary conditions for the spline are obtained by fixing the first derivative at the left- and right-most points of the interval via a three-point finite difference stencil. The chosen interval is  $\sigma \in [0, 170 \text{ MeV}]$ , and in most cases  $n = 40$  grid points are used, with up to 80 points for the computation of the crossover lines. All numerical results obtained in this way have been cross-checked with the Taylor-grid method as outlined in [67]. For the solution of the coupled set of ordinary differential equations (ODEs) an explicit higher-order Runge-Kutta type ODE stepper with adaptive stepsize has been implemented [71].

- 
- [1] A. Bzdak, S. Esumi, V. Koch, J. Liao, M. Stephanov, and N. Xu, *Physics Reports* **853**, 1 (2020).
  - [2] M. G. Alford, A. Schmitt, K. Rajagopal, and T. Schafer, *Rev. Mod. Phys.* **80**, 1455 (2008), [arXiv:0709.4635 \[hep-ph\]](#).
  - [3] M. Buballa and S. Carignano, *Prog. Part. Nucl. Phys.* **81**, 39 (2015), [arXiv:1406.1367 \[hep-ph\]](#).
  - [4] D. Tlusty, 13th Conference on the Intersections of Particle and Nuclear Physics (2018), [arXiv:1810.04767 \[nucl-ex\]](#).
  - [5] V. Klochov (CBM), *Nucl. Phys. A* **1005**, 121945 (2021).
  - [6] A. Butenko, H. Khodzhbagiyani, S. Kostromin, I. Meshkov, A. Sidorin, E. Syresin, G. Trubnikov, and A. Tuzikov, *27th Russian Particle Accelerator Conference* (2021).
  - [7] P. de Forcrand, *PoS LAT2009*, 010 (2009), [arXiv:1005.0539 \[hep-lat\]](#).
  - [8] D. U. Jungnickel and C. Wetterich, *Phys. Rev.* **D53**, 5142 (1996), [arXiv:hep-ph/9505267 \[hep-ph\]](#).
  - [9] B.-J. Schaefer and J. Wambach, *Phys. Part. Nucl.* **39**, 1025 (2008), [arXiv:hep-ph/0611191](#).
  - [10] W.-j. Fu, X. Luo, J. M. Pawłowski, F. Rennecke, R. Wen, and S. Yin, *Phys. Rev. D* **104**, 094047 (2021), [arXiv:2101.06035 \[hep-ph\]](#).
  - [11] W.-j. Fu, J. M. Pawłowski, and F. Rennecke, *Phys. Rev. D* **101**, 054032 (2020), [arXiv:1909.02991 \[hep-ph\]](#).
  - [12] P. Isserstedt, M. Buballa, C. S. Fischer, and P. J. Gunkel, *Phys. Rev. D* **100**, 074011 (2019), [arXiv:1906.11644 \[hep-ph\]](#).
  - [13] C. S. Fischer, *Prog. Part. Nucl. Phys.* **105**, 1 (2019), [arXiv:1810.12938 \[hep-ph\]](#).
  - [14] F. Gao and J. M. Pawłowski, *Phys. Rev. D* **102**, 034027 (2020), [arXiv:2002.07500 \[hep-ph\]](#).
  - [15] F. Gao and J. M. Pawłowski, *Phys. Lett. B* **820**, 136584 (2021), [arXiv:2010.13705 \[hep-ph\]](#).
  - [16] J. Braun and B. Schallmo, [arXiv:2204.00358 \[nucl-th\]](#).
  - [17] J. Braun and B. Schallmo, *Phys. Rev. D* **105**, 036003 (2022), [arXiv:2106.04198 \[hep-ph\]](#).
  - [18] W.-j. Fu, [arXiv:2205.00468 \[hep-ph\]](#).
  - [19] M. Drews and W. Weise, *Phys. Rev. C* **91**, 035802 (2015), [arXiv:1412.7655 \[nucl-th\]](#).
  - [20] K. Otto, M. Oertel, and B.-J. Schaefer, *Phys. Rev. D* **101**, 103021 (2020), [arXiv:1910.11929 \[hep-ph\]](#).
  - [21] K. Otto, M. Oertel, and B.-J. Schaefer, *Eur. Phys. J. ST* **229**, 3629 (2020), [arXiv:2007.07394 \[hep-ph\]](#).
  - [22] M. Leonhardt, M. Pospiech, B. Schallmo, J. Braun, C. Drischler, K. Hebeler, and A. Schwenk, *Phys. Rev. Lett.* **125**, 142502 (2020), [arXiv:1907.05814 \[nucl-th\]](#).
  - [23] B.-J. Schaefer and J. Wambach, *Nucl. Phys. A* **757**, 479 (2005), [arXiv:nucl-th/0403039](#).
  - [24] R.-A. Tripolt, B.-J. Schaefer, L. von Smekal, and J. Wambach, *Phys. Rev.* **D97**, 034022 (2018), [arXiv:1709.05991 \[hep-ph\]](#).
  - [25] R.-A. Tripolt, C. Jung, L. von Smekal, and J. Wambach, *Phys. Rev. D* **104**, 054005 (2021), [arXiv:2105.00861 \[hep-ph\]](#).
  - [26] J. Braun, M. Leonhardt, and M. Pospiech, *Phys. Rev.* **D96**, 076003 (2017), [arXiv:1705.00074 \[hep-ph\]](#).
  - [27] E. Grossi, F. J. Ihssen, J. M. Pawłowski, and N. Wink, *Phys. Rev. D* **104**, 016028 (2021), [arXiv:2102.01602 \[hep-ph\]](#).

- [28] E. Grossi and N. Wink, [arXiv:1903.09503 \[hep-th\]](#).
- [29] Y.-r. Chen, R. Wen, and W.-j. Fu, *Phys. Rev. D* **104**, 054009 (2021), [arXiv:2101.08484 \[hep-ph\]](#).
- [30] J. M. Pawłowski, *Annals Phys.* **322**, 2831 (2007), [arXiv:hep-th/0512261](#).
- [31] H. Gies, *Lect. Notes Phys.* **852**, 287 (2012), [arXiv:hep-ph/0611146 \[hep-ph\]](#).
- [32] J. Braun, *J. Phys. G* **39**, 033001 (2012), [arXiv:1108.4449 \[hep-ph\]](#).
- [33] N. Dupuis, L. Canet, A. Eichhorn, W. Metzner, J. M. Pawłowski, M. Tissier, and N. Wschebor, *Phys. Rept.* **910**, 1 (2021), [arXiv:2006.04853 \[cond-mat.stat-mech\]](#).
- [34] U. Ellwanger, *Z. Phys. C* **62**, 503 (1994), [arXiv:hep-ph/9308260](#).
- [35] T. R. Morris, *Int. J. Mod. Phys. A* **9**, 2411 (1994), [arXiv:hep-ph/9308265](#).
- [36] C. Wetterich, *Phys. Lett.* **B301**, 90 (1993).
- [37] G. De Polsi and N. Wschebor, [arXiv:2204.09170 \[cond-mat.stat-mech\]](#).
- [38] L. Canet, B. Delamotte, D. Mouhanna, and J. Vidal, *Phys. Rev. D* **67**, 065004 (2003), [arXiv:hep-th/0211055](#).
- [39] T. D. Cohen, *Phys. Rev. Lett.* **91**, 222001 (2003), [arXiv:hep-ph/0307089](#).
- [40] G. Markó, U. Reinosa, and Z. Szép, *Phys. Rev. D* **90**, 125021 (2014), [arXiv:1410.6998 \[hep-ph\]](#).
- [41] N. Khan, J. M. Pawłowski, F. Rennecke, and M. M. Scherer, (201), [arXiv:1512.03673 \[hep-ph\]](#).
- [42] W.-j. Fu, J. M. Pawłowski, F. Rennecke, and B.-J. Schaefer, *Phys. Rev. D* **94**, 116020 (2016), [arXiv:1608.04302 \[hep-ph\]](#).
- [43] S. Floerchinger, *JHEP* **05**, 021, [arXiv:1112.4374 \[hep-th\]](#).
- [44] J. M. Pawłowski and N. Strodthoff, *Phys. Rev. D* **92**, 094009 (2015), [arXiv:1508.01160 \[hep-ph\]](#).
- [45] A. J. Helmboldt, J. M. Pawłowski, and N. Strodthoff, *Phys. Rev.* **D91**, 054010 (2015), [arXiv:1409.8414 \[hep-ph\]](#).
- [46] J. Braun, T. Dörfeld, B. Schallmo, and S. Töpfel, *Phys. Rev. D* **104**, 096002 (2021), [arXiv:2008.05978 \[hep-ph\]](#).
- [47] J. Berges, D.-U. Jungnickel, and C. Wetterich, *Eur. Phys. J. C* **13**, 323 (2000), [arXiv:hep-ph/9811347](#).
- [48] B.-J. Schaefer and J. Wambach, *Phys. Rev. D* **75**, 085015 (2007), [arXiv:hep-ph/0603256](#).
- [49] J. Braun, L. Fister, J. M. Pawłowski, and F. Rennecke, *Phys. Rev.* **D94**, 034016 (2016), [arXiv:1412.1045 \[hep-ph\]](#).
- [50] H. Zhang, D. Hou, T. Kojo, and B. Qin, *Phys. Rev.* **D96**, 114029 (2017), [arXiv:1709.05654 \[hep-ph\]](#).
- [51] F. Rennecke and B.-J. Schaefer, *Phys. Rev. D* **96**, 016009 (2017), [arXiv:1610.08748 \[hep-ph\]](#).
- [52] D. F. Litim, *Nucl. Phys. B* **631**, 128 (2002), [arXiv:hep-th/0203006](#).
- [53] D. U. Jungnickel and C. Wetterich, NATO Advanced Study Institute on Confinement, Duality and Nonperturbative Aspects of QCD (1997), [arXiv:hep-ph/9710397](#).
- [54] J. Braun et al., [arXiv:2206.10232 \[hep-th\]](#).
- [55] H. Gies and C. Wetterich, *Phys. Rev. D* **69**, 025001 (2004), [arXiv:hep-th/0209183](#).
- [56] J. Berges, D. U. Jungnickel, and C. Wetterich, *Phys. Rev. D* **59**, 034010 (1999), [arXiv:hep-ph/9705474](#).
- [57] J. Braun, M. Leonhardt, and J. M. Pawłowski, *SciPost Phys.* **6**, 056 (2019), [arXiv:1806.04432 \[hep-ph\]](#).
- [58] B.-J. Schaefer and M. Wagner, *Phys. Rev. D* **79**, 014018 (2009), [arXiv:0808.1491 \[hep-ph\]](#).
- [59] D. F. Litim, *Phys. Lett. B* **486**, 92 (2000), [arXiv:hep-th/0005245](#).
- [60] P. M. Stevenson, *Phys. Rev. D* **23**, 2916 (1981); R. D. Ball, P. E. Haagensen, J. I. Latorre, and E. Moreno, *Phys. Lett. B* **347**, 80 (1995), [arXiv:hep-th/9411122](#).
- [61] L. Canet, *Phys. Rev. B* **71**, 012418 (2005), [arXiv:hep-th/0409300](#).
- [62] G. De Polsi, G. Hernandez-Chifflet, and N. Wschebor, *Phys. Rev. E* **104**, 064101 (2021), [arXiv:2109.14731 \[cond-mat.stat-mech\]](#); G. De Polsi, I. Balog, M. Tissier, and N. Wschebor, *Phys. Rev. E* **101**, 042113 (2020), [arXiv:2001.07525 \[cond-mat.stat-mech\]](#).
- [63] D. F. Litim, *Int. J. Mod. Phys. A* **16**, 2081 (2001), [arXiv:hep-th/0104221](#).
- [64] D. F. Litim, *Phys. Rev. D* **64**, 105007 (2001), [arXiv:hep-th/0103195](#).
- [65] I. Nandori, *JHEP* **04**, 150, [arXiv:1208.5021 \[hep-th\]](#).
- [66] J. M. Pawłowski, M. M. Scherer, R. Schmidt, and S. J. Wetzel, *Annals Phys.* **384**, 165 (2017), [arXiv:1512.03598 \[hep-th\]](#).
- [67] J. A. Adams, J. Berges, S. Bornholdt, F. Freire, N. Tetradis, and C. Wetterich, *Mod. Phys. Lett.* **A10**, 2367 (1995), [arXiv:hep-th/9507093 \[hep-th\]](#); O. Bohr, B.-J. Schaefer, and J. Wambach, *Int. J. Mod. Phys.* **A16**, 3823 (2001), [arXiv:hep-ph/0007098 \[hep-ph\]](#).
- [68] M. Mitter and B.-J. Schaefer, *Phys. Rev.* **D89**, 054027 (2014), [arXiv:1308.3176 \[hep-ph\]](#); S. Resch, F. Rennecke, and B.-J. Schaefer, *Phys. Rev. D* **99**, 076005 (2019), [arXiv:1712.07961 \[hep-ph\]](#).
- [69] J. Borchardt and B. Knorr, *Phys. Rev.* **D94**, 025027 (2016), [arXiv:1603.06726 \[hep-th\]](#).
- [70] A. Koenigstein, M. J. Steil, N. Wink, E. Grossi, J. Braun, M. Buballa, and D. H. Rischke, (), [arXiv:2108.02504 \[cond-mat.stat-mech\]](#); A. Koenigstein, M. J. Steil, N. Wink, E. Grossi, and J. Braun, (), [arXiv:2108.10085 \[cond-mat.stat-mech\]](#); M. J. Steil and A. Koenigstein, [arXiv:2108.04037 \[cond-mat.stat-mech\]](#); J. Stoll, N. Zorbach, A. Koenigstein, M. J. Steil, and S. Rechenberger, [arXiv:2108.10616 \[hep-ph\]](#).
- [71] J. Dormand and P. Prince, *Journal of Computational and Applied Mathematics* **6**, 19 (1980).